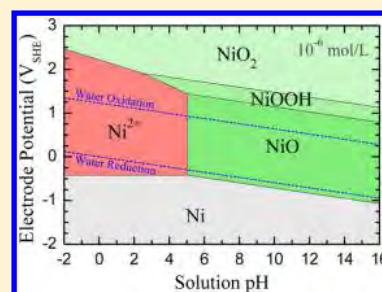


Improved Electrochemical Phase Diagrams from Theory and Experiment: The Ni–Water System and Its Complex Compounds

L.-F. Huang,[†] M. J. Hutchison,[‡] R. J. Santucci, Jr.,[‡] J. R. Scully,[‡] and J. M. Rondinelli^{*,†}[†]Department of Materials Science and Engineering, Northwestern University, Evanston, Illinois 60208, United States[‡]Department of Materials Science and Engineering, University of Virginia, Charlottesville, Virginia 22904, United States

Supporting Information

ABSTRACT: Electrode potential–pH (Pourbaix) diagrams provide a phase map of the most stable compounds of a metal, its corrosion products, and associated ions in solution. The utility of these phase diagrams is that they enable the assessment of electrochemical stabilities, for example, of Ni metal and its derived oxides, hydroxides, and oxyhydroxides, against corrosion in aqueous environments. Remarkably, the Ni Pourbaix diagrams reported over the last 50 years are largely inconsistent with various electrochemical observations, which may be attributed to inaccurate experimental free energies of formation ($\Delta_f G$) for the complex Ni-based compounds used in producing the available diagrams. Here we show that state-of-the-art density-functional theory (DFT) can be used to obtain accurate $\Delta_f G$ values, which lead to Ni Pourbaix diagrams that are more consistent with direct electrochemical experiments: Electrochemical impedance spectroscopy and surface-enhanced Raman spectroscopy are used to characterize the electrochemical stabilities of NiO and Ni(OH)₂ formed on Ni, demonstrating the reliability in correction-free first-principles based Pourbaix diagrams. Our results show the importance in applying modern density functionals in combination with experimental advances in aqueous environment compound identification for assessing electrochemical phase stability of materials, which will be useful for the design, synthesis, and selection of corrosion-resistant metals, photoabsorbers, and photocatalytic materials.



INTRODUCTION

The electrochemical stabilities of materials can be described by their Pourbaix diagrams,^{1–11} which present phase equilibria with respect to electrode potential and solution pH (hydrogen ion activity). First established by Marcel Pourbaix, his atlas of potential–pH diagrams¹ offer a visual representation of the thermodynamic oxidizing and reducing abilities of the major stable oxides, hydroxides, and oxyhydroxides of an element or metal and are used frequently in geochemical and corrosion applications to understand the effects of chemical substitution or addition on phase stability. In the original construction, these diagrams are “calculated” from standard Gibbs free energies of formation, $\Delta_f G$'s, following thermodynamic equilibrium relationships (including Nernst equations, with a given aqueous-ion concentration) over the interested ranges of electrode potential and solution pH.

Pourbaix diagrams for multicomponent compounds are exceedingly complex to simulate and experimentally even more challenging to generate. Simple metals are often equally challenging even in technologically critical transition metals such as Ni, for which various Ni-based alloys, oxides, hydroxides, and ceramics are widely utilized; these compounds exhibit superior mechanical, thermodynamic, electrochemical, electronic, and/or optical properties, which fulfill requirements for biological implants,^{12–14} gas turbine components,^{15–17} irradiation-resistant nuclear alloys,^{18,19} anode materials (e.g., for solid oxide fuel cells,^{20,21} lithium-ion batteries,^{22,23} and capacitors^{24–26}), and photonic and electrochemical cata-

lysts.^{27–29} In all of these applications, the electrochemical stability is a critical factor determining the performance and lifetime of the involved Ni-based materials, especially when operating in aqueous or humid environments.

Ni Pourbaix diagrams have been simulated many times over the last 50 years,^{1,30–32} where the experimental $\Delta_f G$'s are used. However, none of these Ni Pourbaix diagrams are consistent with various electrochemical observations; e.g., NiO and/or Ni(OH)₂ should be stable at pH 5–15,^{24–26,29,33–42} while, in those simulated Ni Pourbaix diagrams with a moderate aqueous ion concentration ($[I] = 10^{-6}$ mol/L), Ni(OH)₂ is only stable at pH of 9–13.^{1,30,31} These failures have important consequences because solutions with pH > 13 are critically important for the synthesis, characterization, and application of Ni (hydr)oxides.^{24–26,29,33–35,41} Furthermore, solutions with pH < 9 are also used to synthesize Ni(OH)₂ from Ni metal using a recent dissolution–precipitation approach.⁴² For these reasons there is a clear technological motivation for possessing accurate Ni Pourbaix diagrams. The apparent inconsistencies suggest inaccuracies in the experimental $\Delta_f G$'s and the resultant Ni Pourbaix diagrams derived from them. Beyond the veracity of the experimental reference energies, these observations further beget the question as to how to assess the accuracy of first-principles computed Pourbaix diagrams. Should they be

Received: March 23, 2017

Revised: April 9, 2017

Published: April 18, 2017

compared to experimentally derived electrode potential–pH diagrams or rather to direct measurements of electrochemical stabilities?

In the experimental determination of thermodynamic data (e.g., $\Delta_f G$'s) for oxides, the combustion heats measured at high temperatures are required,⁴³ where probable measurement error, mass loss, and sample contamination (e.g., by impurities and defects) may cause inaccuracy.⁴³ The atomic bonds in NiO are not very strong, as it has a relatively small $\Delta_f G$ (–1.1 eV/atom at 298.15 K³⁰), only about one-third of those of, e.g., TiO₂, Cr₂O₃, and Al₂O₃.^{43,44} Thus, a high concentration of defects in NiO is unavoidable at high temperatures, which is the reason why as-grown NiO samples obtained by the flame-fusion method have a blackish color rather than a greenish color for pristine NiO.⁴⁵ The experimental $\Delta_f G$ of Ni(OH)₂ is derived from its pH-dependent solubility in experiment,^{46–48} which is also applicable to NiO,⁴⁹ and the accuracy may be influenced by some experimental processes (e.g., solution filtering⁴⁹) and kinetic factors (e.g., finite reaction rate and uncertain degree of hydration). The $\Delta_f G$'s (i.e., chemical potential μ^I) for aqueous ions, e.g., Ni²⁺ and Ni³⁺, are determined from their oxidation or reduction potentials in solution⁵⁰ and can be measured with a relatively high accuracy. Thus, the standard chemical potentials (μ_0^I) for numerous aqueous ions are well archived in many databases.^{50,51}

Here, we show that state-of-the-art density-functional theory (DFT) can be used to calculate accurate $\Delta_f G$'s for Ni compounds (oxides, hydroxide, and oxyhydroxide), which results in reliable Ni Pourbaix diagrams that are systematically consistent with various electrochemical observations in recent decades. We further perform electrochemical impedance spectroscopy (EIS) and surface-enhanced Raman spectroscopy (SERS) measurements to characterize the Ni metal exposed to various buffer solutions (pH 2.9–14). The confirmed electrochemical stabilities of NiO and Ni(OH)₂ formed on Ni are similar to those predicted from our updated Ni Pourbaix diagrams. These results call into question the meaningfulness of directly assessing the accuracy of DFT-calculated Pourbaix diagrams—and whether or not ad hoc corrections are required to reproduce experiment—against experimentally derived ones, especially in cases where the compounds of interest exhibit poor stability and thus possibly high experimental uncertainty in the formation energies. We finally perform probability analyses, which quantitatively reveal the blurring of phase boundaries and the existence of a multiple-phase domain.

METHODS

Computational Approaches. DFT calculations are carried out using the Vienna ab Initio Simulation Package⁵² utilizing the projector augmented-wave method^{53,54} with valence configurations of 3d⁸4s² for Ni, 2s²2p⁴ for O, and 1s¹ for H and a planewave cutoff energy of 600 eV. The HSE06^{55,56} hybrid density-functional is used to treat electronic exchange and correlation. Two sets of reciprocal grids (k' and k'') are required to describe the nonlocal electronic exchange potential in HSE06. The grid-point spacing in the k' grid is $\lesssim 2\pi/20 \text{ \AA}^{-1}$, resulting in an energy convergence of $\lesssim 2 \text{ meV/atom}$. According to the screening length of $\sim 9.4 \text{ \AA}$ for the nonlocal potential in HSE06, the spacing in the k'' grid is set to $\sim 2\pi/9.4 \text{ \AA}^{-1}$. The vibrational frequencies and free energies are calculated using the PHONOPY code,⁵⁷ where the small-displacement method^{58,59} is used (displacement amplitude = 0.03 Å). The PBEsol^{60,61} density functional is used herein to accurately

obtain the vibrational energy.^{44,62} The initial structures are obtained from the *Inorganic Crystal Structure Database*,⁶³ which are fully optimized using both HSE06 and PBEsol. The structural details can be found in the [Supporting Information](#). The energy and force convergence thresholds are 10^{–7} eV and 10^{–3} eV/Å, respectively.

Ni metal and standard O₂ and H₂ gases (298.15 K, 1.0 bar) are used as the references to calculate the free energies of formation ($\Delta_f G$) of the Ni compounds. According to the electrochemical reaction paths connecting all the considered species, the relative chemical potentials ($\Delta\mu$'s) under any electrochemical condition may be calculated using the Nernst equations (see the [Supporting Information](#)). The equilibria domains are determined by comparing the $\Delta\mu$'s among the considered species over the specified electrochemical phase space ($E_{\text{SHE}} \in [-2, 3] \text{ V}$ and $\text{pH} \in [-2, 16]$), leading to the simulated Ni Pourbaix diagram. Additional details of the procedure to generate the Pourbaix diagram are given in ref 44.

Samples and Solutions. Pure Ni (99.99 wt %) samples are prepared using standard metallographic techniques to 1- μm surface finish. Multiple solutions of various pH values (2.9, 4.9, 5.4, 8.4, and 14) of interest are used, where the solutions of pH 4.9, 5.4, and 8.4 are pH-buffered. The initial solutions at pH 2.9, 4.9, and 5.4 are made with [Ni²⁺]’s at 10^{–6}, 10^{–3}, and 10^{–4} mol/L, respectively, using NiCl₂ addition, whereas the Ni²⁺ concentration at pH 8.4 and 14 are not controlled. Details about the specific chemistry of the solutions can be found in the [Supporting Information](#). The solution chemistry is critical, but highly difficult to control especially at the interface of a corroding surface, and is a necessary component of our study. The complexity and variation in solution chemistry arise from the need to control the pH and [Ni²⁺] at various electrochemical conditions. The usages of sulfate, citrate, borate, and triethylamine all depend on achieving the proper pH and Ni²⁺ buffering chemistries, which depend on pH, [Ni²⁺], and composition of solution. All solutions (with the exception of pH 14) are deaerated by bubbling 99.999% N₂ gas for 1 h in the electrochemical cell prior to testing. N₂ gas bubbling persists throughout testing to maintain deaeration.

EIS Measurements. Electrode potential (E), pH, and [Ni²⁺] control are used in combination with electrochemical impedance spectroscopy (EIS) to detect (hydr)oxides at various E –pH conditions. A standard three-electrode electrochemical cell sealed with a knife-edge polytetrafluoroethylene (PTFE) ring (exposed area = 0.8 cm²), with a platinum-mesh counter electrode, is used with saturated calomel or mercury/mercurous sulfate (saturated K₂SO₄) reference electrodes. Experiments at pH 14 are performed in a PTFE cell. Electrode potentials are reported in E_{SHE} . A Gamry Interface 1000 impedance-capable potentiostat is used to control potential for all electrochemical experiments.

The sequence of electrochemical experiments is as follows: for solutions of pH 2.9, 4.9, and 8.4, cathodic polarization (oxide reduction), followed by anodic (oxide formation) potentiostatic EIS (10 mV RMS); for solutions of pH 5.4 and 14, a 1 h anodic polarization is included prior to EIS. Potentiostatic cathodic reduction is performed at –1.76 V_{SHE} in an attempt to reduce air-formed oxides. Anodic potential hold and potentiostatic EIS potentials used here are +0.24 V_{SHE} for solutions of pH 2.9, 5.4, and 8.4, and 0.00 V_{SHE} for solutions of pH 4.9 and 14.

Raman Spectroscopy. Raman spectroscopy is performed ex situ using a 532.06 nm laser with 180° backscattering

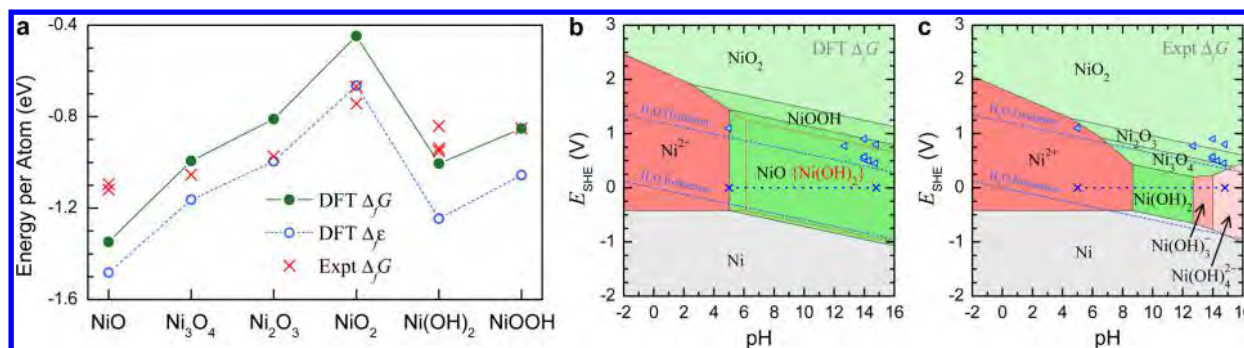


Figure 1. Density-functional theory (DFT) and experimental (Expt) thermodynamic energies and Ni Pourbaix diagrams ($[I] = 10^{-6}$ mol/L, 298.15 K, 1.0 bar). (a) The Expt $\Delta_f G$'s are collected from various databases.^{1,30,51} (b, c) The measured oxidation potentials (blue triangles) and stability ranges (cross-capped dotted blue lines) of $\text{Ni}(\text{OH})_2$ and NiO are indicated; The two parallel inclined lines (blue, broken) indicate the potentials for the oxidation ($2\text{H}_2\text{O} \rightarrow \text{O}_2 + 4\text{H}^+ + 4\text{e}^-$) and reduction ($2\text{H}_2\text{O} + 2\text{e}^- \rightarrow \text{H}_2 + 2\text{OH}^-$) of water. In (b) the phase domain for the metastable $\text{Ni}(\text{OH})_2$ is also indicated by red dashed lines.

geometry on both controls and nickel electrodes tested at various potentials and pH values. Standard NiO and $\text{Ni}(\text{OH})_2$ powders are cold-pressed into pellets for control Raman investigations. Surface-enhanced Raman spectroscopy (SERS) is facilitated where appropriate by ex situ deposition of Ag nanospheres on nickel electrodes post experiment. Electrochemically tested samples are transferred to a solution of 1 mM AgNO_3 and 1 mM HNO_3 and subjected to a cathodic potential of $-0.36 V_{\text{SHE}}$. Depositions are terminated at charges found to yield optimal Raman signal enhancement, typically -20 mC/cm^2 . This deposition procedure follows Oblonsky and Devine's work.⁶⁴ Between all transfers, samples are rinsed with deionized water and dried with compressed lab air. The air-formed oxide arising from air transfer to ex situ Raman studies is investigated as a control. Preapplied and postapplied SERS show no difference in air-formed oxide spectra.

RESULTS AND DISCUSSION

Energetics and Pourbaix Diagrams. Figure 1a shows the free energies of formation, $\Delta_f G$, for the Ni compounds at the standard condition (298.15 K, 1.0 bar) obtained from both our DFT calculations and previous experimental estimation,^{1,30,51} as well as the DFT electronic formation energies, $\Delta_f \epsilon$. To calculate $\Delta_f \epsilon$ using DFT, only the electronic energies of the Ni compounds (oxides, hydroxide, and oxyhydroxide) and reference species (Ni metal, O_2 molecule, and H_2 molecule) are used, while to calculate $\Delta_f G$, we additionally include the DFT vibrational free energies, as well as the molecular translational and rotational free energies in standard O_2 and H_2 gases measured from experiment.⁴³ We note that the HSE06 (refs 55, 56) hybrid-density functional used here for $\Delta_f \epsilon$ includes the screened nonlocal exact electronic exchange interaction, which improves the accuracy of the calculated electronic structure of solids,⁶⁵ especially transition-metal compounds with localized d electrons.^{66–68} The PBEsol^{60,61} functional is used to obtain the vibrational free energies, which is both efficient and accurate in capturing various thermal effects.^{44,62}

The DFT $\Delta_f G$'s are higher than the corresponding $\Delta_f \epsilon$'s by $\lesssim 0.25$ eV/atom (Figure 1a), quantitatively showing the importance of the vibrational, translational, and rotational free energy contributions required for accurate thermodynamical simulation. More numerical details about these energies are listed in the Supporting Information. The DFT and experimental (Expt) $\Delta_f G$'s exhibit the same qualitative chemical

trend; e.g., the oxide $\Delta_f G$ increases with O content, and $\text{Ni}(\text{OH})_2$ has a lower $\Delta_f G$ than NiOOH . However, we discern a discrepancy of $\lesssim 0.30$ eV/atom between these two groups of $\Delta_f G$'s, which may result in remarkably different electrochemical stabilities of these Ni compounds as we show next.

In the simulation of Ni Pourbaix diagram, the chemical potential of a solid Ni compound (μ^s) equals its $\Delta_f G$, and the concentration-dependent aqueous-ion chemical potential (μ^l) is calculated using $\mu^l = \mu_0^l + RT \ln([I])$, where R is the gas constant and μ_0^l is the chemical potential of ion I at the standard condition (298.15 K, 1.0 bar, 1.0 mol/L, and pH 0). The μ_0^l 's for the considered aqueous ions (Ni^{2+} , Ni^{3+} , NiOH^+ , $\text{Ni}(\text{OH})_3^-$, and $\text{Ni}(\text{OH})_4^{2-}$) are obtained from various experimental databases.^{1,30,50,51} In solution, $[I]$ normally varies between the orders of 10^{-8} and 10^{-4} mol/L,^{14,30,69} and a moderate $[I]$ of 10^{-6} mol/L is considered in this section. Results with variable $[I]$ will be discussed in the next section. The relative electrochemical stabilities between the involved solids and aqueous ions at any solution pH and electrode potential E_{SHE} (referring to the standard hydrogen electrode) are described by the chemical potentials of reaction ($\Delta\mu$'s) for the reaction paths that connect all the considered species (see the Supporting Information). The determination of the phase equilibria at any pH and E_{SHE} according to the calculated $\Delta\mu(\text{pH}, E_{\text{SHE}})$'s leads to a Ni Pourbaix diagram, as shown in Figure 1b or 1c.

The DFT $\Delta\mu$ of NiO is lower than that of $\text{Ni}(\text{OH})_2$ by 0.13 eV. For this reason, $\text{Ni}(\text{OH})_2$ would appear as a metastable phase in the Ni Pourbaix diagram as indicated by the red text in brackets in Figure 1b, and the phase domain (red dotted lines) appears when the more stable NiO is excluded in the simulation. The calculated stabilities of NiO and $\text{Ni}(\text{OH})_2$ against dissolution (into Ni^{2+}), oxidation (into NiOOH), and reduction (into Ni) are clearly demarcated by their phase domains in Figure 1b. Moreover, NiO and $\text{Ni}(\text{OH})_2$ are stable at $\text{pH} \gtrsim 5.0$ and 6.1, respectively, below which they will dissolve into Ni^{2+} ions. They are also stable at any achievable alkaline pH, when E_{SHE} resides between the oxidation and reduction potentials of water.

In stark contrast, upon using the $\Delta\mu$'s derived from the experimental $\Delta_f G$'s, we find that $\text{Ni}(\text{OH})_2$ becomes more stable than NiO by 0.08 eV on average, and $\text{Ni}(\text{OH})_2$ exhibits a considerably smaller phase domain (than that in the DFT diagram, Figure 1b) with two dissolution boundaries at pH 8.7 and 12.7 (Figure 1c). Furthermore, the two dissolution

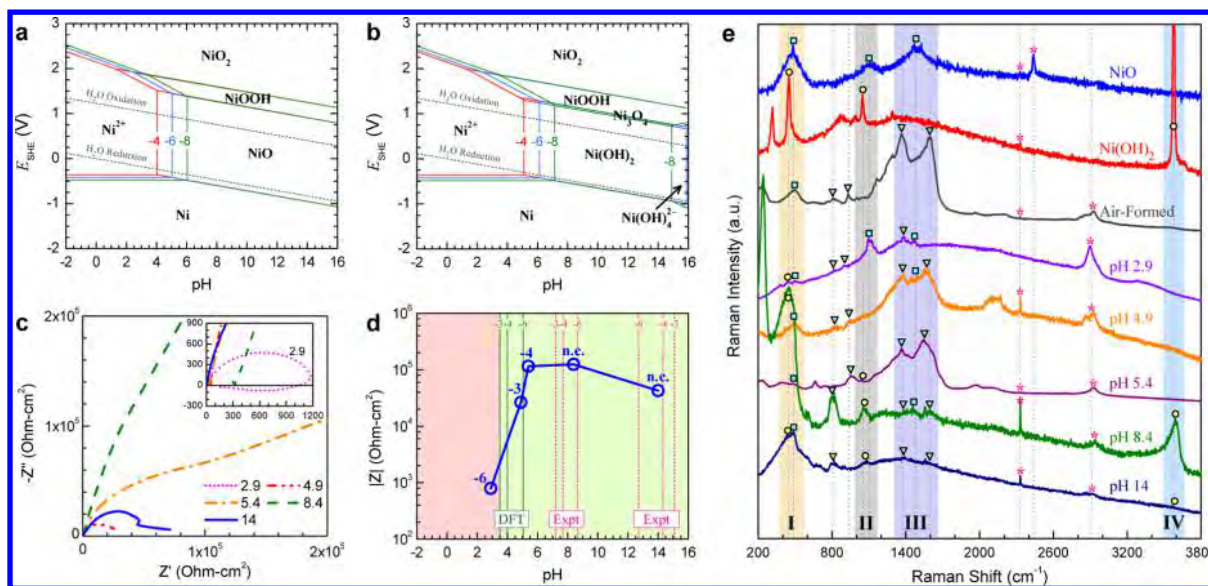


Figure 2. Calculated DFT Ni Pourbaix diagrams at different aqueous ion concentrations and experimental EIS and SERS measurements. (a, b) $[I]$ varies from 10^{-8} to 10^{-4} mol/L. (c) Nyquist plots (voltage frequency $\omega = 10^5 \sim 10^{-3}$ Hz) of the measured electrochemical impedances for the Ni samples exposed to solutions at pH 2.9–14, and the inset zooms depict the pH = 2.9 result. (d) The measured pH-dependent $|Z|$ ($\omega = 10^{-2}$ Hz) is compared with the simulated dissolution boundaries of NiO/Ni(OH)₂ using the DFT and experimental $\Delta_f G$'s for Ni compounds, where the $[I]$ values of $10^{-6} \sim 10^{-3}$ mol/L and those not controlled (n.c. $[I]$ values) are also indicated. (e) The Ni samples exposed to air and solutions (pH 2.9–14) are measured using SERS, and the standard NiO and Ni(OH)₂ samples are measured by standard Raman spectroscopy, where the Raman peaks from NiO, Ni(OH)₂, air-formed NiO, and unclear sources are labeled by squares, circles, triangles, and stars, respectively. Four shaded regions (I, II, III, and IV) are considered in our analysis.

boundaries of the metastable NiO at pH 9.1 and 11.9 (not shown) significantly differ from those obtained at the DFT level. Although Ni(OH)₂ is more frequently reported in experiment,^{24–26,29,70} NiO and Ni(OH)₂ probably coexist in many electrochemical experiments^{36–39} due to their close $\Delta\mu$'s and the fact that it is challenging to completely differentiate them using conventional experimental methods (e.g., Raman spectroscopy).³⁹ Importantly, NiO, Ni(OH)₂, or the “NiO + Ni(OH)₂” complex is observed to be stable at pH 5–14.8 in numerous experiments,^{24–26,29,33,34,36–40} where pH 14.8 corresponds to the highest alkaline solution ever reported. These observations are much more consistent with the phase domains of NiO and Ni(OH)₂ obtained from our DFT-derived Pourbaix diagram based on calculated $\Delta_f G$'s (Figure 1b) whereas the Pourbaix diagram constructed from experimental $\Delta_f G$'s (Figure 1c) shows that the phase domains (electrochemical stabilities) are largely underestimated and do not persist up to such high alkalinity. Furthermore, the average oxidation potentials for the Ni(OH)₂ → NiOOH transition measured in different solutions^{24–26,29,33,36–39} also reside around the phase boundary of Ni(OH)₂ in our DFT Pourbaix diagram. In contrast the oxidation potential for Ni(OH)₂ is systematically lower than the measured ones by ~ 0.4 V, and the oxidant NiOOH is replaced by Ni₃O₄ and Ni₂O₃ that have large phase areas in the experimental Pourbaix diagram (Figure 1c). It should be noted that some kinetic factors may contribute to the scatter in the experimental data for the Ni(OH)₂ → NiOOH oxidation potential (Figure 1b and c); e.g., the oxidation potential is dependent on the electrode-potential scan rate used in the electrochemical cycling measurements.^{24–26} Furthermore, the Ni(OH)₂ samples measured in those experiments correspond to the disordered hydrous α -Ni(OH)₂, and after a long-term aging or electrochemical cycling, it will slowly transform into the more stable crystalline anhydrous (or

less hydrous) β -Ni(OH)₂^{33,35,39,41,71} that is calculated here. Thus, it is reasonable that the β -Ni(OH)₂ → NiOOH oxidation potential in the DFT Pourbaix diagram is slightly larger (by $\lesssim 0.3$ V) than most of the α -Ni(OH)₂ → NiOOH oxidation potentials measured in experiment (Figure 1b).

Apart from the electrochemical stabilities of NiO and Ni(OH)₂ against corrosion and oxidation, additional experimental phenomena also support our calculated relative electrochemical stabilities between NiO and Ni(OH)₂. X-ray photoelectron spectroscopy (XPS) experiments report that NiO grows underneath the outer Ni(OH)₂ layer during the passivation processes of Ni and Fe₅₃Ni surfaces in an alkaline solution (1.0 mol/L NaOH),³⁶ and NiO may grow faster than Ni(OH)₂ on Cu₅₀Ni under a high enough electrode potential.³⁸ It also has been observed that when the NiO ratio in the “NiO + Ni(OH)₂” complex increases, the electrochemical stability of the oxide also increases because the transition into NiOOH becomes less favorable. These observations indicate that NiO may have a higher thermodynamic stability than Ni(OH)₂ under various electrochemical conditions, while the earlier formation of Ni(OH)₂ may be due to its higher kinetic activity. The thermodynamic conclusion is consistent with these rankings from our DFT calculations, i.e., $\Delta\mu$ (NiO < Ni(OH)₂), while the experimental phase diagram suggests a reversal of these relative stabilities. In addition, it is also well-known that heating can readily promote the Ni(OH)₂ → NiO transition,^{24–26,30,70} thus, their relative stabilities may become more apparent in electrochemical experiments with varying temperature, where XPS may be used to characterize the phase fractions of NiO and Ni(OH)₂, as well as their temperature dependencies.

EIS and SERS Measurements. Aqueous ions, especially Ni²⁺, are not always measured or controlled in corrosion experiments. However, the stabilities of Ni metal and

Table 1. Summary of our Experimental Findings, Comparing the Simulation Results Using the DFT and Expt $\Delta_f G$'s for Ni Compounds^a

pH	E_{SHE} (V)	[I] (mol/L)	EIS	SERS	DFT	Expt
2.9	0.24	10^{-6}	active dissolution	AF oxide	Ni^{2+}	Ni^{2+}
4.9	0.00	10^{-3}	passive dissolution	AF + EF oxide	$\text{NiO} + \text{Ni}(\text{OH})_2$	Ni^{2+}
5.4	0.24	10^{-4}	passive dissolution	AF + EF oxide	$\text{NiO} + \text{Ni}(\text{OH})_2$	Ni^{2+}
8.4	0.24	n.c.	passive dissolution	AF + EF (hydr)oxide	$\text{NiO} + \text{Ni}(\text{OH})_2$	$\text{Ni}(\text{OH})_2 + \text{NiO} + \text{Ni}^{2+}$
14	0.00	n.c.	passive dissolution	AF + EF (hydr)oxide	$\text{NiO} + \text{Ni}(\text{OH})_2$	$\text{Ni}(\text{OH})_3^- + \text{Ni}(\text{OH})_4^{2-}$

^aAt pH 8.4 and 14, the experimental [I]'s are not controlled (n.c.), and the moderate [I] of 10^{-6} mol/L is used for those simulation results.

compounds against corrosion will be sensitive to [I]. Thus, the variation of the Ni Pourbaix diagram with [I] requires a quantitative understanding, and with this nuance, it also becomes necessary to perform advanced electrochemical experiments with precisely controlled [I]. Here, we use electrochemical impedance spectroscopy (EIS) and surface-enhanced Raman spectroscopy (SERS) to characterize the formation of NiO and Ni(OH)₂ on Ni samples exposed to various buffer solutions (pH 2.9–14) with controlled [Ni²⁺] as appropriate.

First, the variations of the DFT Ni Pourbaix diagrams at 298.15 K with [I] ranging from 10^{-8} to 10^{-4} mol/L are shown in Figure 2a and 2b, which include the phase domains for the stable NiO and the metastable Ni(OH)₂ compounds, respectively. It can be seen that at $E_{\text{SHE}} \sim 0$ V, both NiO and Ni(OH)₂ are stable against dissolution in any alkaline solution (pH > 7), except for the dissolution of Ni(OH)₂ into Ni(OH)₄²⁻ ions at pH $\gtrsim 14.9$ and [I] = 10^{-8} mol/L (Figure 2b). Note that pH = 14.9 and [I] = 10^{-8} mol/L correspond to a highly alkaline and dilute solution, respectively, which is rarely achieved in experiment. Thus, we can conclude that in any alkaline solution, Ni metal tends to be protected by the passivating NiO and/or Ni(OH)₂ layer grown on surface. In acidic solution, on the other hand, the dissolution boundaries of NiO and Ni(OH)₂ reside at pH 4.0–6.0 and 5.1–7.1, respectively, where the boundary pH increases by 1.0 with decreasing [I] by 100 times. Such dissolution-boundary variation with [I] is highly useful to understand the results measured in our electrochemical experiments as we show next.

In an EIS measurement, the obtained impedance (Z) is a complex quantity and depends on the voltage frequency (ω), which can be expressed as $Z(\omega) = Z'(\omega) + iZ''(\omega)$. When there is a passivating layer formed on the surface of Ni metal, a large Z is expected at low frequencies. The plots of the Z' – Z'' relationships, i.e., Nyquist plots, for the Ni samples exposed to various solution pH (2.9–14) are shown in Figure 2c, where ω varies from 10^5 to 10^{-3} Hz, and E_{SHE} is either 0.00 or 0.24 V. Both Z' and Z'' are negligibly small at high frequencies (e.g., 10^5 Hz), and Z' generally increases with decreasing ω , except for the nonmonotonic Z' at pH 2.9 (Figure 2c, inset). The variation of $|Z(\omega)|$ ($=\sqrt{Z'^2 + Z''^2}$) at a low ω (10^{-2} Hz) with solution pH is shown in Figure 2d, which is compared with the dissolution boundaries of NiO in both the Pourbaix diagrams based on the DFT and experimental Ni compound free energies of formations.

According to the small $|Z|$ at pH 2.9 (Figure 2c and 2d), we can conclude that there is no stable oxide/hydroxide layer protecting the Ni metal surface from active dissolution, which is consistent with the results derived from both the DFT and Expt $\Delta_f G$'s (Figure 2d). With increasing solution pH, $|Z|$ substantially increases between pH 2.9 and 4.9 and then

persists at a high level above pH 4.9. This indicates that at the controlled ion concentrations (10^{-6} – 10^{-3}), the dissolution boundary of the passivating layer formed on Ni metal should be at pH $\lesssim 4.9$. These EIS results are highly consistent with the DFT NiO–Ni²⁺ boundaries residing at pH 3.5–5.0 (Figure 2d), whereas the Pourbaix diagram using the experimental $\Delta_f G$ values predicts Ni(OH)₂–Ni²⁺ boundaries at pH 7.2–8.7 which are considerably different from the EIS results.

The passivating layers formed on the Ni samples, which are exposed to the considered solutions (see Table 1), are further characterized using ex situ SERS, as shown in Figure 2e. To understand the SERS results for the electrochemically formed (EF) NiO and Ni(OH)₂, measurements using regular Raman spectroscopy on standard NiO and Ni(OH)₂ samples as well as the SERS measurement on a Ni sample with air-formed (AF) NiO are also provided for comparison. The most discernible Raman peaks observed in NiO, Ni(OH)₂, and the AF NiO on Ni are labeled by squares, circles, and triangles, respectively. Although AF NiO has some common Raman peaks consistent with the standard NiO, e.g., at 494 cm⁻¹, it also exclusively has many distinct peaks, which may be due to the optical influence from NiO–Ni and NiO–Ag interfaces or due to the SERS technique itself. The origins for the peaks at 2400 and 2900 cm⁻¹, labeled by stars, are unclear and may arise from residual water molecules. Indeed, the measured SERS spectra are always complicated by various possible factors, e.g., the (hydr)oxide–metal interface,^{72,73} presence of water molecules,⁷⁴ and any uncertainty in experimental sample morphology. Therefore, to facilitate the phase identification and analysis of NiO and/or Ni(OH)₂ on Ni metal, we only focus on four frequency regions (I, II, III, IV, as shaded in Figure 2e), where the different electrochemically treated samples share common peaks.

In the SERS spectrum for the Ni sample exposed to solution with pH 2.9, the main Raman peaks observed in the I–III regions are similar to the corresponding peaks from the standard and AF NiO. Also, the O–H stretching mode observed in Ni(OH)₂ at a high frequency (3800 cm⁻¹, IV region) cannot be seen. Referring to the EIS results above, it is clear that the NiO characterized here is spontaneously formed in air and is not a consequence of the electrochemical process. At pH from 4.9 to 14, the Raman peaks in regions I–III are similar to those from the standard and AF NiO. As they are clearly observed, both the AF and EF NiO are present. The O–H stretching mode at 3800 cm⁻¹ becomes observable in the Raman spectra for pH 8.4 and 14, where the other peaks ascribed to Ni(OH)₂ are also more obvious therein than those at pH 4.9 and 5.4. This phenomenon can be explained using our DFT Ni Pourbaix diagram presented in Figure 2b (i.e., [I] = 10^{-4} mol/L), where the electrochemical stability of Ni(OH)₂ should be low at pH values of 2.9 or 4.9, close to or lower than its dissolution-boundary at pH ~ 5.0 .

The experimental findings from our EIS and SERS measurements are summarized in Table 1, which are compared with the results derived from the simulated Ni Pourbaix diagrams using DFT and experimental free energies of formation. Considering that NiO and Ni(OH)₂ have nearly degenerate relative chemical potentials, $\Delta\mu$, both within our DFT and extracted from the experimental energies, they are always written together as possible coexisting passivating species in Table 1 (e.g., the DFT results at pH \gtrsim 4.9). When the solution pH resides at a phase boundary, the equilibria species of the adjoining domains are also included in Table 1 (e.g., the experimental results at pH 8.4 and 14). According to the EIS and SERS measurements, Ni actively corrodes in the solution at pH 2.9 ([I] = 10⁻⁶ mol/L) but will be passivated by the EF NiO and Ni(OH)₂ layers in solutions at pH 4.9–14 ([I] = 10⁻⁴ ~ 10⁻³ mol/L or not controlled). Similar conclusions can be derived from our DFT Ni Pourbaix diagrams, where the “NiO + Ni(OH)₂” complex is stable at pH \gtrsim 4.9. However, the experimental Ni Pourbaix diagrams lead to largely underestimated stabilities of the “NiO + Ni(OH)₂” complex and predict that Ni always actively corrodes except for a partial passivation at pH 8.4 contrary to our electrochemical measurements.

Phase Probability Analysis. Based on our accurate DFT free energies and calculated Ni Pourbaix diagrams, we now propose a useful electrochemical analysis approach based on kinetically limited phase coexistence near the boundary. At any phase boundary in a Pourbaix diagram, the thermodynamic probabilities of the relevant species should vary continuously between 0 and 1, resulting in a physically blurred boundary. The probability can be expressed as

$$P_i = \frac{\exp\left(-\frac{\Delta\mu_i}{k_B T}\right)}{\sum_j \exp\left(-\frac{\Delta\mu_j}{k_B T}\right)} \quad (1)$$

where i and j index the species, k_B is the Boltzmann constant, and T (=298.15 K) is the temperature. Here we use [I] = 10⁻⁶ mol/L to calculate the chemical potentials of aqueous ions. The variations in the probability of observing different species, $P_{\{i\}}$, with respect to pH (at $E_{\text{SHE}} = 0$) and to E_{SHE} (at pH = 7) are shown in Figure 3.

From the calculated probability profiles, we deduce two important facts: (1) a thermodynamic blurring of the phase boundaries and (2) the existence of multiple phases at the NiO–NiOOH boundary. When solution pH or E_{SHE} goes beyond the stability domain of a Ni compound, e.g., NiO at the NiO–Ni²⁺ boundary in Figure 3a, the P_{NiO} decreases exponentially. Within a pH range of 0.5 away from the phase boundary, NiO still has a finite precipitation probability of \gtrsim 0.1. The P_{NiO} decreases drastically with E_{SHE} (Figure 3b), and a P_{NiO} of 0.1 corresponds to a small deviation (\lesssim 0.05 V) of E_{SHE} away from the NiO phase boundary. Furthermore, at the NiO–NiOOH phase boundary, there are observable precipitation probabilities for Ni₃O₄ and Ni₂O₃, as well as NiO, NiOOH, Ni(OH)₂, and NiO₂ extending from their phase domains (Figure 3b). In the electrochemical measurement of the NiO → NiOOH or Ni(OH)₂ → NiOOH oxidation potential, the phase transition is triggered by increasing E_{SHE} . The existence of multiple phases at the NiO–NiOOH boundary may complicate the transition process and could contribute to the discrepancy in the experimental oxidation potentials (Figure 1).

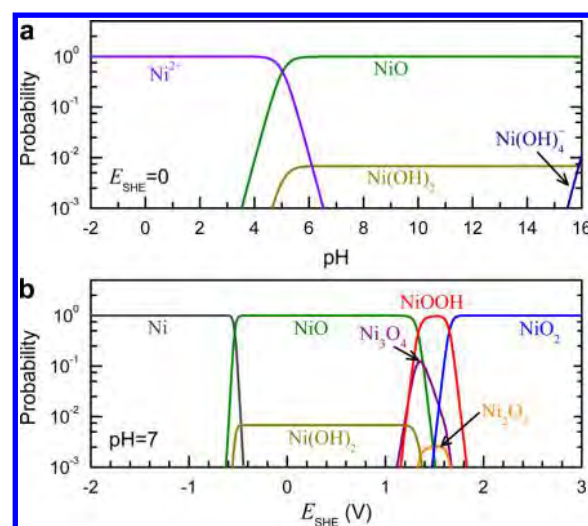


Figure 3. Probability profiles for various species at different electrochemical conditions. (a, b) The probability variations with pH at $E_{\text{SHE}} = 0$ V (a) and with E_{SHE} at pH = 7 (b) are considered.

CONCLUSION

We constructed an accurate Ni Pourbaix diagram using state-of-the-art first-principles calculations in combination with modern electrochemical measurements to resolve inconsistencies among observed electrochemical phenomena since the first formulation of the diagram more than 50 years ago. The previously reported Ni Pourbaix diagrams all largely underestimate the electrochemical stabilities of NiO and Ni(OH)₂ when compared to various electrochemical observations. This is caused by erroneous experimental free energies of formations for Ni compounds used therein; those errors may originate from many possible physical and technical sources (e.g., defect contamination, complex processes, or experimental uncertainties). We further used EIS and SERS to characterize Ni exposed to various solutions at pH 2.9–14, and measured pH-dependent electrochemical stabilities of NiO and Ni(OH)₂ closely validate the high accuracy of our DFT-based Ni Pourbaix diagrams. We finally implemented an additional probability analysis, which further reveals the thermodynamic blurring of phase boundaries and the existence of a multiple-phase domains at the NiO–NiOOH boundary.

The accurate DFT $\Delta_f G$'s and Ni Pourbaix diagrams, the combined theory-experiment approach, and the electrochemical analyses presented in this work will be useful for understanding and exploiting various Ni-based materials. More generally, our results indicate that a sophisticated treatment of transition-metal compounds using density-functional approaches is required. The strict accuracy comparison of Pourbaix diagrams obtained from computationally cheap functionals to reproduce experimental Pourbaix diagrams may lead to errant conclusions owing to intrinsic inaccuracies among the experimental formation energies used to construct the experimental diagrams, especially when observed electrochemical oxidation and reduction processes are inconsistent with the experimental phase diagram. Therefore, we hope this work motivate the reinvestigation of many reported potential–pH diagrams through detailed simulation and experiment.

■ ASSOCIATED CONTENT

■ Supporting Information

The Supporting Information is available free of charge on the ACS Publications website at DOI: 10.1021/acs.jpcc.7b02771.

Structural details, thermodynamic formula and energies, electrochemical reaction paths and chemical potentials of reaction, and chemical details of buffer solutions (PDF)

■ AUTHOR INFORMATION

Corresponding Author

*E-mail: jrondinelli@northwestern.edu.

ORCID

L.-F. Huang: 0000-0003-2937-5183

J. M. Rondinelli: 0000-0003-0508-2175

Notes

The authors declare no competing financial interest.

■ ACKNOWLEDGMENTS

L.-F.H. and J.M.R. thank Prof. L.D. Marks, Dr. X.-X. Yu, and Mr. E. Tennesen at Northwestern University for helpful discussions with them. The authors were supported by the Office of Naval Research Grant No. N00014-14-1-0675 and NSF Grant No. DMR-1309999. Calculations were performed using the QUEST HPC Facility at Northwestern University, the HPCMP facilities at the Navy DSRC, the Extreme Science and Engineering Discovery Environment (NSF, Grant No. ACI-1053575), and the CARBON cluster at the Center for Nanoscale Materials in Argonne National Laboratory (DOE-BES, Grant No. DE-AC02-06CH11357).

■ REFERENCES

- (1) Pourbaix, M. *ATLAS of Electrochemical Equilibria in Aqueous Solutions*; Pergamon Press: Oxford, 1966.
- (2) Hansen, H. A.; Rossmel, J.; Nørskov, J. K. Surface Pourbaix diagrams and oxygen reduction activity of Pt, Ag, and Ni(111) surfaces studied by DFT. *Phys. Chem. Chem. Phys.* **2008**, *10*, 3722–3730.
- (3) Taylor, C. D.; Neurock, M.; Scully, J. R. First-principles investigation of the fundamental corrosion properties of a model Cu₃₈ nanoparticle and the (111), (113) surfaces. *J. Electrochem. Soc.* **2008**, *155*, C407–C414.
- (4) Tang, L.; Li, X.; Cammarata, R. C.; Friesen, C.; Sieradzki, K. Electrochemical stability of elemental metal nanoparticles. *J. Am. Chem. Soc.* **2010**, *132*, 11722–11726.
- (5) Tang, L.; Han, B.; Persson, K.; Friesen, C.; He, T.; Sieradzki, K.; Ceder, G. Electrochemical stability of nanometer-scale Pt particles in acidic environments. *J. Am. Chem. Soc.* **2010**, *132*, 596–600.
- (6) Persson, K. A.; Waldwick, B.; Lazic, P.; Ceder, G. Prediction of solid-aqueous equilibria: Scheme to combine first-principles calculations of solids with experimental aqueous states. *Phys. Rev. B: Condens. Matter Mater. Phys.* **2012**, *85*, 235438.
- (7) Castelli, I. E.; Thygesen, K. S.; Jacobsen, K. W. Calculated Pourbaix diagrams of cubic perovskites for water splitting: Stability against corrosion. *Top. Catal.* **2014**, *57*, 265–272.
- (8) Todorova, M.; Neugebauer, J. Extending the concept of defect chemistry from semiconductor physics to electrochemistry. *Phys. Rev. Appl.* **2014**, *1*, 014001.
- (9) Zeng, Z.; Chan, M. K. Y.; Zhao, Z. J.; Kubal, J.; Fan, D.; Greeley, J. Towards first principles-based prediction of highly accurate electrochemical pourbaix diagrams. *J. Phys. Chem. C* **2015**, *119*, 18177–18187.
- (10) Todorova, M.; Neugebauer, J. Identification of bulk oxide defects in an electrochemical environment. *Faraday Discuss.* **2015**, *180*, 97–112.
- (11) Todorova, M.; Neugebauer, J. Connecting semiconductor defect chemistry with electrochemistry: Impact of the electrolyte on the formation and concentration of point defects in ZnO. *Surf. Sci.* **2015**, *631*, 190–195.
- (12) Hoar, T. P.; Mears, D. C. Corrosion-resistant alloys in chloride solutions: materials for surgical implants. *Proc. R. Soc. London, Ser. A* **1966**, *294*, 486–510.
- (13) Pourbaix, M. Electrochemical corrosion of metallic biomaterials. *Biomaterials* **1984**, *5*, 122–134.
- (14) Jacobs, J. J.; Gilbert, J. L.; Urban, R. M. Corrosion of metal orthopaedic implants. *J. Bone Joint Surg.* **1998**, *80*, 268–282.
- (15) Goward, G. W. Progress in coatings for gas turbine airfoils. *Surf. Coat. Technol.* **1998**, *108109*, 73–79.
- (16) Eliaz, N.; Shemesh, G.; Latanision, R. M. Hot corrosion in gas turbine components. *Eng. Failure Anal.* **2002**, *9*, 31–43.
- (17) Pomeroy, M. J. Coatings for gas turbine materials and long term stability issues. *Mater. Eng.* **2005**, *26*, 223–231. Special Issue: Tribology.
- (18) Zinkle, S. J.; Busby, J. T. Structural materials for fission and fusion energy. *Mater. Today* **2009**, *12*, 12–19.
- (19) Zinkle, S. J.; Snead, L. L. Designing radiation resistance in materials for fusion energy. *Annu. Rev. Mater. Res.* **2014**, *44*, 241–267.
- (20) Sarantaridis, D.; Atkinson, A. Redox cycling of Ni-based solid oxide fuel cell anodes: A review. *Fuel Cells* **2007**, *7*, 246–258.
- (21) Wang, W.; Su, C.; Wu, Y.; Ran, R.; Shao, Z. Progress in solid oxide fuel cells with nickel-based anodes operating on methane and related fuels. *Chem. Rev.* **2013**, *113*, 8104–8151.
- (22) Poizot, P.; Laruelle, S.; Grugeon, S.; Dupont, L.; Tarascon, J. M. Nano-sized transition-metal oxides as negative-electrode materials for lithium-ion batteries. *Nature* **2000**, *407*, 496–499.
- (23) Kvasa, A.; Azaceta, E.; Leonet, O.; Bengoechea, M.; Boyano, I.; Tena-Zaera, R.; de Meaza, I.; Miguel, O.; Grande, H.-J.; Blazquez, J. A. Ni/NiO based 3D core-shell foam anode for lithium ion batteries. *Electrochim. Acta* **2015**, *180*, 16–21.
- (24) Wu, Q.; Wen, M.; Chen, S.; Wu, Q. Lamellar-crossing-structured Ni(OH)₂/CNTs/Ni(OH)₂ nanocomposite for electrochemical supercapacitor materials. *J. Alloys Compd.* **2015**, *646*, 990–997.
- (25) Chen, J. S.; Gui, Y.; Blackwood, D. J. A versatile ionic liquid-assisted approach to synthesize hierarchical structures of β-Ni(OH)₂ nanosheets for high performance pseudocapacitor. *Electrochim. Acta* **2016**, *188*, 863–870.
- (26) Abbas, S. A.; Jung, K. D. Preparation of mesoporous microspheres of NiO with high surface area and analysis on their pseudocapacitive behavior. *Electrochim. Acta* **2016**, *193*, 145–153.
- (27) Nolan, M.; Long, R.; English, N. J.; Mooney, D. A. Hybrid density functional theory description of N- and C-doping of NiO. *J. Chem. Phys.* **2011**, *134*, 224703.
- (28) Wang, J.; Higashihara, T. Effects of catalyst loading amount on the synthesis of poly(3-hexylthiophene) via externally initiated Kumada catalyst-transfer polycondensation. *Front. Mater. Sci.* **2014**, *8*, 383–390.
- (29) Qin, M.; Maza, W. A.; Stratakes, B. M.; Ahrenholtz, S. R.; Morris, A. J.; He, Z. Nanoparticulate Ni(OH)₂ films synthesized from macrocyclic nickel(II) Cyclam for hydrogen production in microbial electrolytic cells. *J. Electrochem. Soc.* **2016**, *163*, F437–F442.
- (30) Beverskog, B.; Puigdomenech, I. Revised pourbaix diagrams for nickel at 25–300 °C. *Corros. Sci.* **1997**, *39*, 969–980.
- (31) Muñoz-Portero, M. J.; García-Antón, J.; Guiñón, J. L.; Pérez-Herranz, V. Pourbaix diagrams for nickel in concentrated aqueous lithium bromide solutions at 25 °C. *Corrosion* **2007**, *63*, 625–634.
- (32) Cook, W. G.; Olive, R. P. Pourbaix diagrams for the nickel-water system extended to high-supercritical and low-supercritical conditions. *Corros. Sci.* **2012**, *58*, 284–290.
- (33) Schreiber-Guzmán, R. S.; Vilche, J. R.; Arví, A. J. The kinetics and mechanism of the nickel electrode-III. The potentiodynamic response of nickel electrodes in alkaline solutions in the potential region of Ni(OH)₂ formation. *Corros. Sci.* **1978**, *18*, 765–778.

- (34) Melendres, C. A.; Xu, S. In situ laser Raman spectroscopic study of anodic corrosion films on nickel and cobalt. *J. Electrochem. Soc.* **1984**, *131*, 2239–2243.
- (35) Corrigan, D. A. The catalysis of the oxygen evolution reaction by iron impurities in thin film nickel oxide electrodes. *J. Electrochem. Soc.* **1987**, *134*, 377–384.
- (36) Hoppe, H.-W.; Strehblow, H.-H. XPS and UPS examinations of passive layers on Ni and Fe₅₃Ni alloys. *Corros. Sci.* **1990**, *31*, 167–177.
- (37) Druska, P.; Strehblow, H. H.; Golledge, S. A surface analytical examination of passive layers on CuNi alloys: Part I. Alkaline solution. *Corros. Sci.* **1996**, *38*, 835–851.
- (38) Druska, P.; Strehblow, H.-H. Surface analytical examination of passive layers on Cu–Ni alloys Part II. Acidic solutions. *Corros. Sci.* **1996**, *38*, 1369–1383.
- (39) Lo, Y. L.; Hwang, B. J. In situ Raman studies on cathodically deposited nickel hydroxide films and electroless Ni–P electrodes in 1 M KOH solution. *Langmuir* **1998**, *14*, 944–950.
- (40) Lillard, R. S.; Scully, J. R. Electrochemical passivation of ordered NiAl. *J. Electrochem. Soc.* **1998**, *145*, 2024–2032.
- (41) Trotochaud, L.; Young, S. L.; Ranney, J. K.; Boettcher, S. W. Nickel–iron oxyhydroxide oxygen-evolution electrocatalysts: The role of intentional and incidental iron incorporation. *J. Am. Chem. Soc.* **2014**, *136*, 6744–6753.
- (42) Jung, S. C.; Sim, S. L.; Soon, Y. W.; Lim, C. M.; Hing, P.; Jennings, J. R. Synthesis of nanostructured β -Ni(OH)₂ by electrochemical dissolution-precipitation and its application as a water oxidation catalyst. *Nanotechnology* **2016**, *27*, 275401.
- (43) Chase, M. W. *NIST-JANAF Thermochemical Tables*, 4th ed.; American Institute of Physics: New York, 1998.
- (44) Huang, L.-F.; Rondinelli, J. M. Electrochemical phase diagrams for Ti oxides from density functional calculations. *Phys. Rev. B: Condens. Matter Mater. Phys.* **2015**, *92*, 245126.
- (45) Mochizuki, S.; Saito, T. Intrinsic and defect-related luminescence of NiO. *Phys. B* **2009**, *404*, 4850–4853. Proceedings of the 25th International Conference on Defects in Semiconductors.
- (46) Gayer, K. H.; Garrett, A. B. The equilibrium of nickel hydroxide, Ni(OH)₂, in solutions of hydrochloric acid and sodium hydroxide at 25°. *J. Am. Chem. Soc.* **1949**, *71*, 2973–2975.
- (47) Chickerur, N. S.; Sabat, B. B.; Mahapatra, P. P. Solubility and thermodynamic data of nickel hydroxide. *Thermochim. Acta* **1980**, *41*, 375–377.
- (48) Mattigod, S. V.; Rai, D.; Felmy, A. R.; Rao, L. Solubility and solubility product of crystalline Ni(OH)₂. *J. Solution Chem.* **1997**, *26*, 391–403.
- (49) Tremaine, P. R.; Leblanc, J. C. The solubility of nickel oxide and hydrolysis of Ni²⁺ in water to 573 K. *J. Chem. Thermodyn.* **1980**, *12*, 521–538.
- (50) Burgess, J. *Metal Ions in Solution*; Ellis Horwood Limited: Chichester, 1978.
- (51) Bard, A. J.; Parsons, R.; Jordan, J. *Standard Potentials in Aqueous Solution*; Marcel Dekker: New York, 1985.
- (52) Hafner, J. Ab-initio simulations of materials using VASP: Density-functional theory and beyond. *J. Comput. Chem.* **2008**, *29*, 2044–2078.
- (53) Blöchl, P. E. Projector augmented-wave method. *Phys. Rev. B: Condens. Matter Mater. Phys.* **1994**, *50*, 17953–17979.
- (54) Kresse, G.; Joubert, D. From ultrasoft pseudopotentials to the projector augmented-wave method. *Phys. Rev. B: Condens. Matter Mater. Phys.* **1999**, *59*, 1758–1775.
- (55) Heyd, J.; Scuseria, G. E.; Ernzerhof, M. Erratum: “Hybrid functionals based on a screened Coulomb potential” [*J. Chem. Phys.* **118**, 8207 (2003)]. *J. Chem. Phys.* **2006**, *124*, 219906.
- (56) Vydrov, O. A.; Heyd, J.; Krukau, A. V.; Scuseria, G. E. Importance of short-range versus long-range Hartree-Fock exchange for the performance of hybrid density functionals. *J. Chem. Phys.* **2006**, *125*, 074106.
- (57) Togo, A.; Tanaka, I. First principles phonon calculations in materials science. *Scr. Mater.* **2015**, *108*, 1–5.
- (58) Kresse, G.; Furthmüller, J.; Hafner, J. Ab initio force constant approach to phonon dispersion relations of diamond and graphite. *Europhys. Lett.* **1995**, *32*, 729.
- (59) Parlinski, K.; Li, Z. Q.; Kawazoe, Y. First-principles determination of the soft mode in cubic ZrO₂. *Phys. Rev. Lett.* **1997**, *78*, 4063–4066.
- (60) Perdew, J. P.; Ruzsinszky, A.; Csonka, G. I.; Vydrov, O. A.; Scuseria, G. E.; Constantin, L. A.; Zhou, X.; Burke, K. Restoring the density-gradient expansion for exchange in solids and surfaces. *Phys. Rev. Lett.* **2008**, *100*, 136406.
- (61) Perdew, J. P.; Ruzsinszky, A.; Csonka, G. I.; Vydrov, O. A.; Scuseria, G. E.; Constantin, L. A.; Zhou, X.; Burke, K. Erratum: restoring the density-gradient expansion for exchange in solids and surfaces [*Phys. Rev. Lett.* **100**, 136406 (2008)]. *Phys. Rev. Lett.* **2009**, *102*, 039902.
- (62) Huang, L. F.; Lu, X. Z.; Tennesen, E.; Rondinelli, J. M. An efficient ab-initio quasiharmonic approach for the thermodynamics of solids. *Comput. Mater. Sci.* **2016**, *120*, 84–93.
- (63) Belsky, A.; Hellenbrandt, M.; Karen, V. L.; Luksch, P. New developments in the Inorganic Crystal Structure Database (ICSD): Accessibility in support of materials research and design. *Acta Crystallogr., Sect. B: Struct. Sci.* **2002**, *58*, 364–369.
- (64) Oblonsky, L. J.; Devine, T. M. A surface enhanced Raman spectroscopic study of the passive films formed in borate buffer on iron, nickel, chromium, and stainless steel. *Corros. Sci.* **1995**, *37*, 17–41.
- (65) Paier, J.; Marsman, M.; Hummer, K.; Kresse, G.; Gerber, I. C.; Ángyán, J. G. Screened hybrid density functionals applied to solids. *J. Chem. Phys.* **2006**, *124*, 154709.
- (66) Franchini, C.; Podloucky, R.; Paier, J.; Marsman, M.; Kresse, G. Ground-state properties of multivalent manganese oxides: Density functional and hybrid density functional calculations. *Phys. Rev. B: Condens. Matter Mater. Phys.* **2007**, *75*, 195128.
- (67) Chevrier, V. L.; Ong, S. P.; Armiento, R.; Chan, M. K. Y.; Ceder, G. Hybrid density functional calculations of redox potentials and formation energies of transition metal compounds. *Phys. Rev. B: Condens. Matter Mater. Phys.* **2010**, *82*, 075122.
- (68) Yan, J.; Nørskov, J. K. Calculated formation and reaction energies of 3d transition metal oxides using a hierarchy of exchange-correlation functionals. *Phys. Rev. B: Condens. Matter Mater. Phys.* **2013**, *88*, 245204.
- (69) Beverskog, B.; Puigdomenech, I. Revised pourbaix diagrams for copper at 25 to 300 °C. *J. Electrochem. Soc.* **1997**, *144*, 3476–3483.
- (70) Han, S. Y.; Lee, D. H.; Chang, Y. J.; Ryu, S. O.; Lee, T. J.; Chang, C. H. The growth mechanism of nickel oxide thin films by room-temperature chemical bath deposition. *J. Electrochem. Soc.* **2006**, *153*, C382–C386.
- (71) Klaus, S.; Cai, Y.; Louie, M. W.; Trotochaud, L.; Bell, A. T. Effects of Fe electrolyte impurities on Ni(OH)₂/NiOOH structure and oxygen evolution activity. *J. Phys. Chem. C* **2015**, *119*, 7243–7254.
- (72) Wu, D.-Y.; Liu, X.-M.; Huang, Y.-F.; Ren, B.; Xu, X.; Tian, Z.-Q. Surface catalytic coupling reaction of p-mercaptoaniline linking to silver nanostructures responsible for abnormal SERS enhancement: A DFT study. *J. Phys. Chem. C* **2009**, *113*, 18212–18222.
- (73) Wang, A.; Huang, Y.-F.; Sur, U. K.; Wu, D.-Y.; Ren, B.; Rondinelli, S.; Amatore, C.; Tian, Z.-Q. In situ identification of intermediates of benzyl chloride reduction at a silver electrode by SERS coupled with DFT calculations. *J. Am. Chem. Soc.* **2010**, *132*, 9534–9536.
- (74) Li, J.-F.; Huang, Y.-F.; Duan, S.; Pang, R.; Wu, D.-Y.; Ren, B.; Xu, X.; Tian, Z.-Q. SERS and DFT study of water on metal cathodes of silver, gold, and platinum nanoparticles. *Phys. Chem. Chem. Phys.* **2010**, *12*, 2493–2502.